Effects of Shot Sleeve Pre-solidification on the Microstructure and Tensile Properties of High Pressure Die Cast AE44

WENHAO YU, HONGYI ZHAN, and CHRISTOPHER M. GOURLAY

In cold-chamber high pressure die casting (HPDC), some pre-solidification occurs in the shot sleeve prior to being injected into the die cavity. Here, we study the effects of pre-solidification on the development of microstructure and defects in the HPDC of magnesium alloy AE44 (Mg–4Al–4RE–0.2Mn, wt pct, where RE are mixed La and Ce) and on subsequent tensile properties. Samples with a high fraction of pre-solidification contained both externally solidified crystals (ESCs) and cold flakes, which also induced large pockets of positive macrosegregation. Variations in the morphology and length scale of α-Mg grains and eutectic $Al_{11}RE_3$ are discussed in terms of the different cooling conditions for each microstructural feature using a grain morphology map for α-Mg. A high fraction of pre-solidification resulted in a small decrease in yield stress due to the larger microstructural length scale, and a substantial decrease in ultimate tensile strength and ductility due to the presence of a non-bonded interface between cold flakes and the surrounding material. The results provide insights into microstructure formation in the HPDC of AE44 and highlight the importance of controlling the extent of pre-solidification that is injected into the die cavity.

I. INTRODUCTION

COLD-CHAMBER high pressure die casting (HPDC) is one of the most effective fabrication methods for magnesium alloys in the automotive industry, as it can mass produce complex-shaped, thin-walled components, with a high degree of accuracy and repeatability.[1,2] In cold-chamber HPDC, heat loss within the colder shot sleeve results in some pre-solidification before the alloy is shot into the die cavity.[3–11] Two types of pre-solidification can form: externally solidified crystals (ESCs) and cold flakes.[5,6,12–16]

ESCs are single crystal equiaxed dendrites that nucleate and grow in the liquid in the shot sleeve prior to injection into the die cavity. In the final casting, ESCs are often dendrite fragments, due to their fragmentation in the turbulent flow during the fast shot stage. The fraction of ESCs formed in the shot sleeve can be reduced by taking steps to reduce the loss of superheat prior to injection, for example by increasing the initial melt superheat, the fill fraction and/or the temperature of the chamber walls and plunger tip,[6,13,17] or adjusting the biscuit thickness,[18] or the filling delay time.[19]

In contrast, cold flakes are large polycrystalline flakes in the final casting that originally formed as a solidified layer on the shot sleeve wall before being torn off by the plunger and injected into the die cavity.[5,12] Cold flakes have a flat side where they contacted the shot sleeve and, since a lubricant is usually applied to the surface of the shot sleeve, cold flakes usually have a non-bonded interface between their flat side and the in-cavity solidified microstructure.[12] Most past work on cold flakes has been on aluminium alloys. Studies on Al–Si alloys have shown that the presence of cold flakes reduces the ductility and UTS and increases the variability in these properties, but does not significantly impact the yield stress.[20–23] Two broad strategies are often taken to eliminate cold flakes in HPDC: (i) reducing pre-solidification in the shot sleeve by raising the pouring temperature,[12,24] maintaining a high temperature in the shot sleeve,[25,26] and/or developing shot sleeve designs that minimise heat loss[27]; and (ii) impeding cold flakes from entering the main cavity and keeping them in the biscuit and runner through die design optimisation.[12,28,29]

Much less research has investigated cold flakes in magnesium alloys, particularly in newer alloys such as AE44 (Mg–4Al–4RE in wt pct where RE is rare earth

WENHAO YU and CHRISTOPHER. M. GOURLAY are with the Department of Materials, Imperial College London, London SW7 2AZ, UK. Contact e-mail: wy1615@ic.ac.uk HONGYI ZHAN is with the China Science Lab, General Motors Global Research and Development, Shanghai 201206, P.R. China.

mischmetal). AE-series magnesium alloys were developed as high pressure die casting alloys with good creep resistance at 125 °C to 200 °C[30–32] which is a requirement of automotive powertrain components.[33–35] In recent years, AE44 has found increasing application due to a combination of cost, processing and property factors including: the availability of relatively low cost two component La + Ce mischmetal,[36] the good melt handleability and castability of AE44 in the HPDC process,[37] and AE44 being among the best creep resistant magnesium alloys[38] with adequate corrosion performance.[39,40] AE44 is also heat treatable by a T5 treatment which increases the yield strength by ~10 pct at ambient temperature.[36,41,42]

In this work, we investigate how shot sleeve pre-solidification in HPDC AE44 affects microstructure and defect formation, including both the α-Mg phase and the majority intermetallic compound $Al_{11}RE_3$. We then explore how shot sleeve pre-solidification affects tensile properties in the as-cast and T5 conditions in this alloy.

II. METHODS

To study samples with different levels of pre-solidification, we used the HPDC die in Figure 1 that produces multiple tensile test bars where the bar at position A produces a high fraction of pre-solidified material and the bar at position B a low fraction of pre-solidified material. The bars at both positions had the same dimensions, with a gauge length of 50 mm and diameter of 8 mm. The difference in pre-solidification at the two bar positions arises from their different distances to the biscuit and the die design. Bar A (with high pre-solidification content) is filled with material that entered the die cavity in the latter stages of die filling and, therefore, is material that was nearer the water-cooled plunger where a higher fraction of pre-solidification occurred.[6] Additionally, the geometry of the gate and runner results in different flow paths before each test bar which affects the extent to which cold flakes are blocked from entering the test bar. The alloy composition of the AE44-2 used in this study is given in Table I. The alloy

was cast by an LK-280T cold-chamber HPDC machine. The alloy melt was held at 710 °C ± 10 °C before being ladled into the shot sleeve pre heated to 200 °C. The shot sleeve filling time was optimised to 2.53 seconds. The melt was then injected into the cavity, with the plunger speed set to 0.15 m/s in the low-speed stage, and 3.7 m/s in the fast-speed stage. The temperature of the cavity wall was held at 170 °C to 190 °C. Castings were manually removed from the cavity and quenched in water.

20 test bars were kept at the as-cast condition and 20 were given a T5 heat treatment of 250 °C for 4 hours. The tensile tests were carried out at room temperature on an Instron 5982 tensile testing machine, at a strain rate of 10^{-4} s^{-1}. The fracture surfaces were investigated by a stereo-optical microscope and a scanning electron microscope (SEM). After that, the fracture surface was cut longitudinally, and another portion of the test bar was cut transversely. Both the longitudinal and transverse-sectioned samples were ground to 4000 grit SiC paper and polished with a solution of 20 pct OPS and 80 pct ethanol. To lightly etch the microstructure, samples were etched in a solution of 200 ml ethylene glycol, 68 ml distilled water, 80 ml acetic acid and 4 ml nitric acid for 4 seconds. To expose the 3D structure of the intermetallic phases, 10 pct nitric acid in water was used to deep etch the Mg.

SEM imaging and electron backscattered diffraction (EBSD) mapping was performed on a Zeiss Sigma-300 SEM with a Bruker e-FlashHR detector, operated at 20kV, 15mm working distance with a 70 deg tilted stage. Bruker Quantax Esprit 2.1 software was used to acquire and index EBSD patterns. Focused ion beam (FIB) serial sectioning was performed on a Zeiss Auriga cross-beam SEM equipped with a FIB using 36 deg tilt angle, at 30kV with a working distance of 5 mm, to maintain an appropriate slice spacing. The slice interval was 70 nm and the milling current was 1 nA. The 2D images from FIB slices were aligned, cropped, and processed by an anisotropic diffusion filter in ImageJ.[43] The stack of BSD images was loaded into the 'Avizo 9.3' software, where they were filtered and segmented into binary images based on the Z-contrast of $Al_{11}RE_3$, allowing the $Al_{11}RE_3$ phase to be reconstructed into 3D. The volume fraction of $Al_{11}RE_3$ was then measured in Avizo 9.3 from the occupied voxels.

III. RESULTS AND DISCUSSION

A. Effects of Pre-solidification on α-Mg Microstructure

The effects of shot sleeve pre-solidification on the general α-Mg microstructure are overviewed in Figure 2 at low magnification. Figure 2(a) shows the typical microstructure of low pre-solidification content samples from bar B which contain the typical HPDC features of defect bands (dark solute-rich bands), a surface layer, and a small area fraction of ESCs with little or no discernible porosity. Comparing with past work on HPDC magnesium alloys, note that the defect bands in
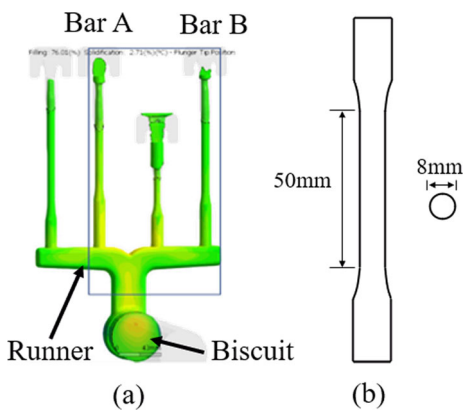

Fig. 1—(a) Schematic diagram of the HPDC part indicating the two bars used for characterisation. (b) Dimensions of the bar with a gauge length of 50 mm and diameter of 8 mm.

Table I. Chemical Composition of Experimental Alloy (Weight Percent) Obtained by Optical Emission Spectroscopy

	Mg	Al	La	Ce	Mn	Si	Zn	Cu	Fe	Ni
AE44-2	bal.	3.69	1.23	2.63	0.18	0.024	0.0074	0.0011	0.001	0.0005
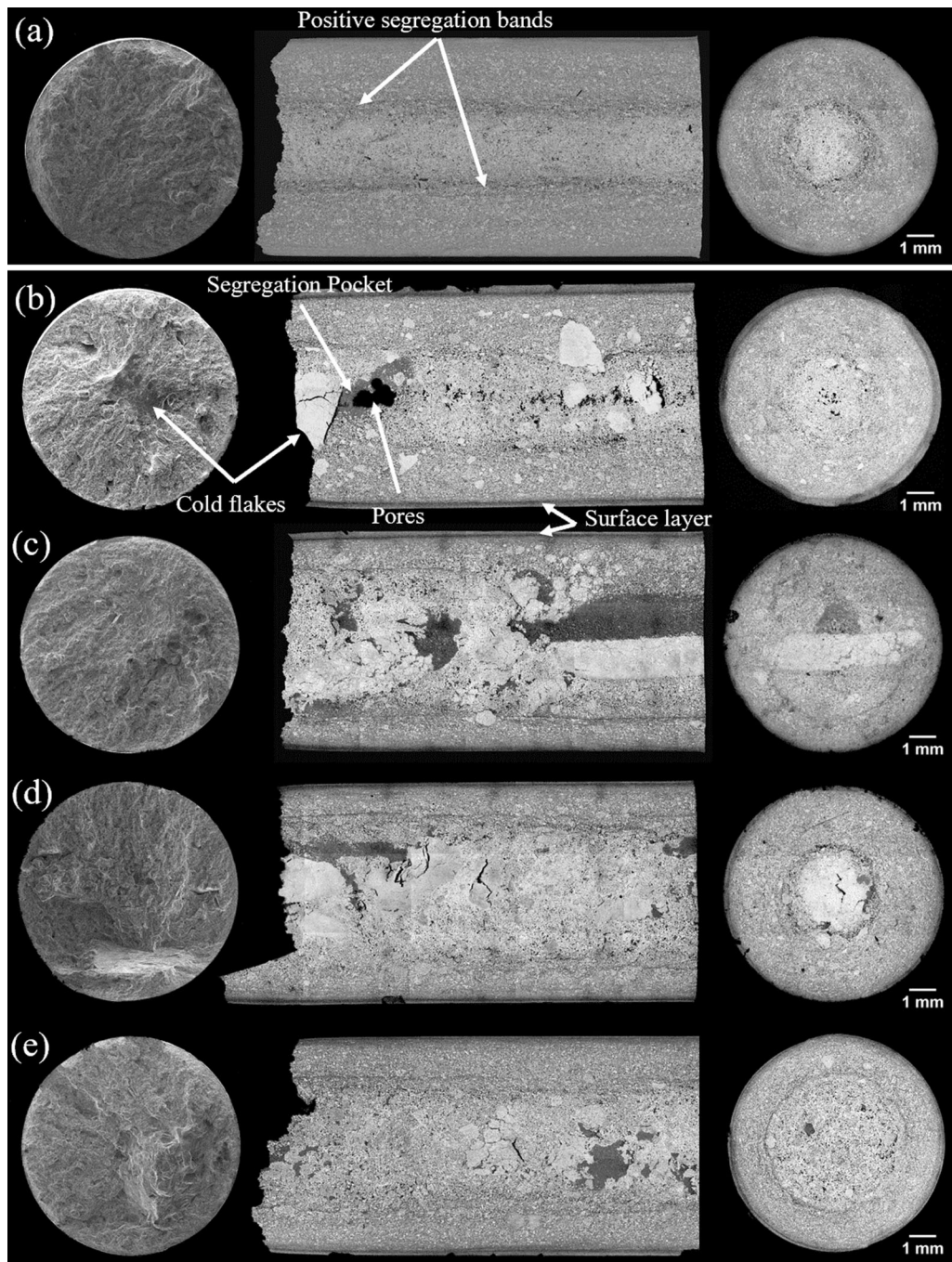
Fig. 2—Typical microstructures of HPDC AE44 after tensile testing. (*a*) Low pre-solidification content sample from bar B. (*b*) through (*e*) Four different high pre-solidification content samples from bar A. Left: SEM images of the fracture surface. Middle: OM images of etched longitudinal sections with the fracture surface on the left side. Right: OM images of etched transverse cross-sections.

these AE44 castings contained mostly positive macrosegregation whereas past work on HPDC tensile bars in AM20/50/60 and AZ91 usually had porosity in addition to positive macrosegregation in defect bands.[7,17,44,45] This is likely to be due to the higher eutectic fraction in AE44 (∼34 pct *vs* ∼14 pct in

AZ91[46]) since past work on HPDC Al–Si alloys[47] has shown that increasing the eutectic fraction reduces microporosity in defect bands.

Figures 2(b) through (e) shows typical microstructures of the high pre-solidification content samples from bar A, with a large area fraction of fragmented ESCs and large cold flakes. The cold flakes have strongly influenced microstructure formation. For example, the positive macrosegregation bands have been disrupted and their courses changed by cold flakes, and the cold flakes induced the formation of large pockets of positive macrosegregation (which appear as large dark grey areas at the low magnification shown in Figure 2) that occasionally also contained large pores as labelled in Figure 2(b).

Figure 3 provides more detail of the microstructure within cold flakes. Figures 3(a) through (d) show cold flakes are polycrystalline with multiple grain orientations. From the EBSD orientation maps in Figures 3(c) and (d), we see that the α-Mg grain size in cold flakes is considerably larger than the in-cavity grain size. Table II lists the measured grain size and the secondary dendrite arm spacing (SDAS) of α-Mg in different features. The average grain size of α-Mg in cold flakes is more than ten times larger than the in-cavity grains. Figure 3(d) contains a large cold flake with the non-bonded interface at the bottom where variations in grain size are evident. The grain size within five large cold flakes was measured as a function of the distance from the non-bonded interface and plotted in Figure 3(e). The grain size in cold flakes increases gradually with distance from the non-bonded interface until about 1000 μm. The grains within cold flakes are elongated near to the non-bonded interface and, beyond 1000 μm, the grains have more equiaxed structure with a grain size of approximately 220 μm.

Figure 3(f) shows the α-Mg dendrite structure within a cold flake near the non-bonded interface. The secondary dendrite arm spacing (SDAS) was measured as a function of distance from the non-bonded interface and is plotted in Figure 3(g). The SDAS increased gradually away from the non-bonded interface from 2 μm to about 10 μm. The SDAS, λ_2, is related to the local solidification time, t_f, with an expression of $\lambda_2 = kt_f^n$,[48,49] where k is a constant, and n is around 0.33 for Mg alloys.[49–51] Since the local solidification time is inversely proportional to the average cooling rate during solidification, we see that the fine SDAS at the surface of the cold flake is due to initial fast cooling at the interface with the shot sleeve wall and the increasing SDAS away from the cold flake surface indicates a slowing cooling rate with continued growth.

Figure 4 overviews the α-Mg microstructure of the near-surface region in samples with and without cold flakes. Figures 4(a) and (b) are from a typical low pre-solidification content sample where fine grains can be seen near the surface and fragmented ESCs in material more than 200μm from the casting surface. Figures 4(c) and (d) are from a typical high pre-solidification content sample where the fraction of ESCs is

much higher. Figure 4(e) summarizes the area fraction of pre-solidified material at different locations. The high pre-solidification content samples contain about two times more pre-solidification product near the surface and about 50 pct more in the centre regions than the low pre-solidification content samples, on average. Comparing Figures 4(a) and (b) with (c) and (d), the presence of a higher fraction of ESCs generates a significantly more nonuniform and heterogeneous microstructure, even in regions such as these with no cold flakes.

It was found here that cold flakes could significantly affect ESCs. The typical features of ESCs located away from any cold flakes are overviewed in Figures 5(a) through (c). This ESC fragment is a $\sim$ 450 μm long dendrite surrounded by in-cavity solidified grains. From the EBSD IPF-X map, this ESC is a single crystal of α-Mg. In contrast, regions containing cold flakes often had some ESCs entrapped within the cold flakes, such as the example in Figure 5(d). These entrapped ESCs were often full dendrites rather than fragments. It can be seen that the positions of the entrapped ESCs are close to the non-bonded interface. Figure 5(e) summarizes the grain size of fragmented ESCs and entrapped ESCs, showing the substantially larger grain size of ESCs entrapped within cold flakes than those surrounded by in-cavity-solidified grains. This occurs because the entrapped ESCs are protected from fragmentation during die filling, keeping ESCs as large dendrites which increases the heterogeneity of the microstructure and increases the grain size of entrapped ESCs up to 550 μm. The presence of ESCs entrapped within cold flakes shows that these ESCs were present prior to the formation of this cold flake.

Macrosegregation pockets with a length scale of millimetres formed near to cold flakes and were absent in samples without cold flakes. Macrosegregation pockets appear as large dark regions after etching in low magnification OM images such as those in Figures 2(b) through (d). Figure 6(a) is the same cross-section as Figure 2(e) and is shown at higher magnification in Figures 6(b) and (c), demonstrating that these pockets contain a mixture of α-Mg dendrites and eutectic, and appear dark at low magnification because they contain a higher fraction of eutectic than surrounding regions. They are thus regions of positive macrosegregation. The α-Mg grains in segregation pockets were fine dendrites, Figure 6(c), with a significantly different morphology to the ESCs, grains in cold flakes and the in-cavity grains. Figures 6(d) and (e) shows an SEM image and EBSD orientation map of a typical positive segregation pocket. The α-Mg in the segregation pocket is polycrystalline with equiaxed grains that are significantly larger than the surrounding grains, as quantified in Table II.

The formation of segregation pockets seems to be related to semi-solid rheology and interactions between the cold flakes and in-cavity solidifying grains during filling and/or feeding. Despite the very different length and time scales, there is a partial analogy here with large icebergs travelling through an ice floe field in the sea driven by water currents and wind, where large 'leads' of ice-free water develop behind translating and rotating icebergs.[52] In HPDC, since this occurs in the mushy
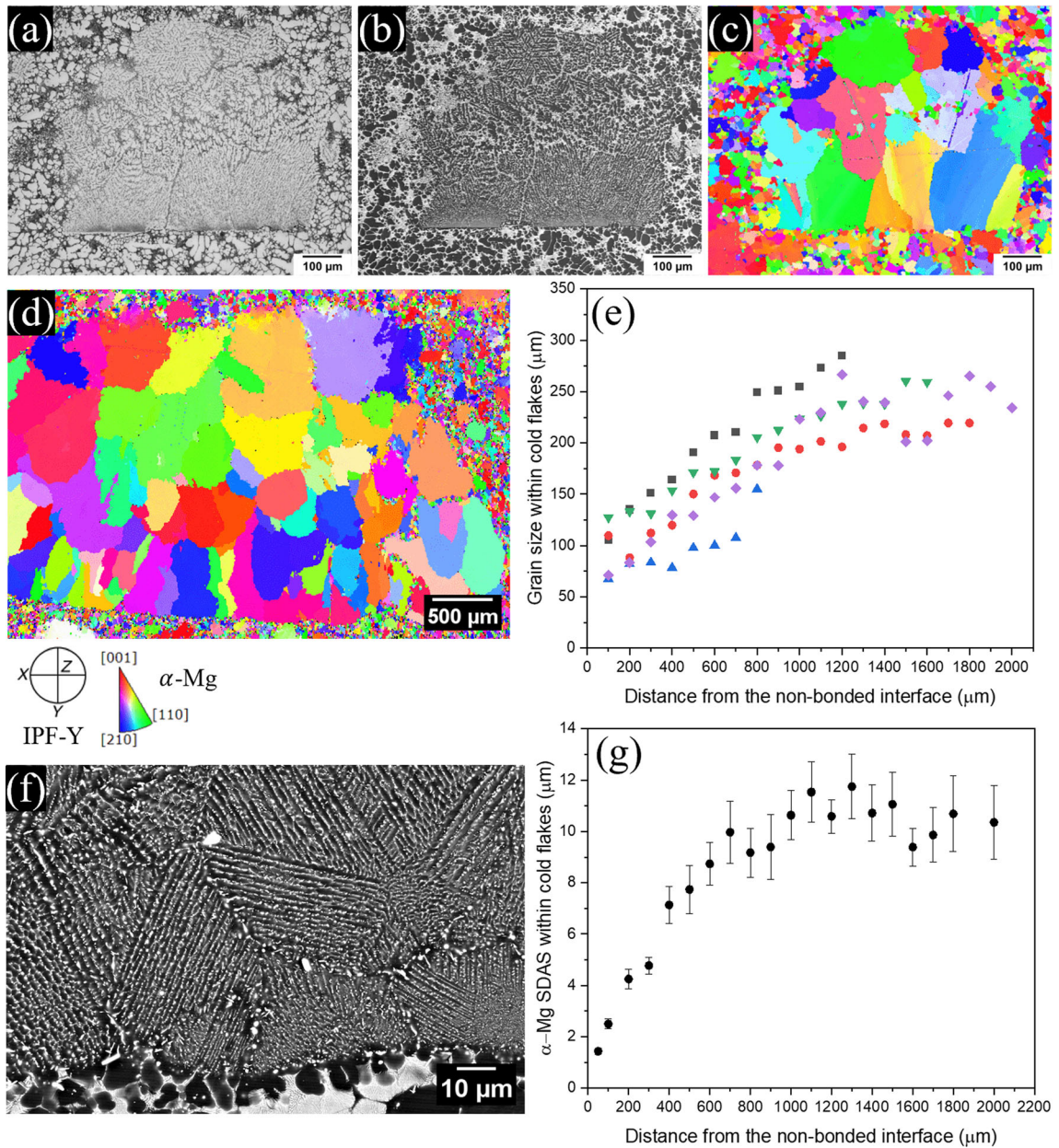
Fig. 3—Typical microstructure within cold flakes. (*a*) through (*c*) OM image, BSE image, and EBSD orientation map (IPF-Y) respectively of the same cold flake. (*d*) IPF-Y EBSD map of another cold flake with a non-bonded interface at the bottom. (*e*) the α-Mg grain size in cold flakes as a function of distance from the non-bonded interface. Each colour represents a different cold flake. (*f*) SE image showing the dendrite arms within a cold flake. The non-bonded interface is at the bottom. (*g*) SDAS of α-Mg within cold flakes as a function of distance from the non-bonded interface. The 95 pct confidence interval is included as a vertical-axis error bar.

Table II.   α-Mg Grain Size and SDAS in Different Features

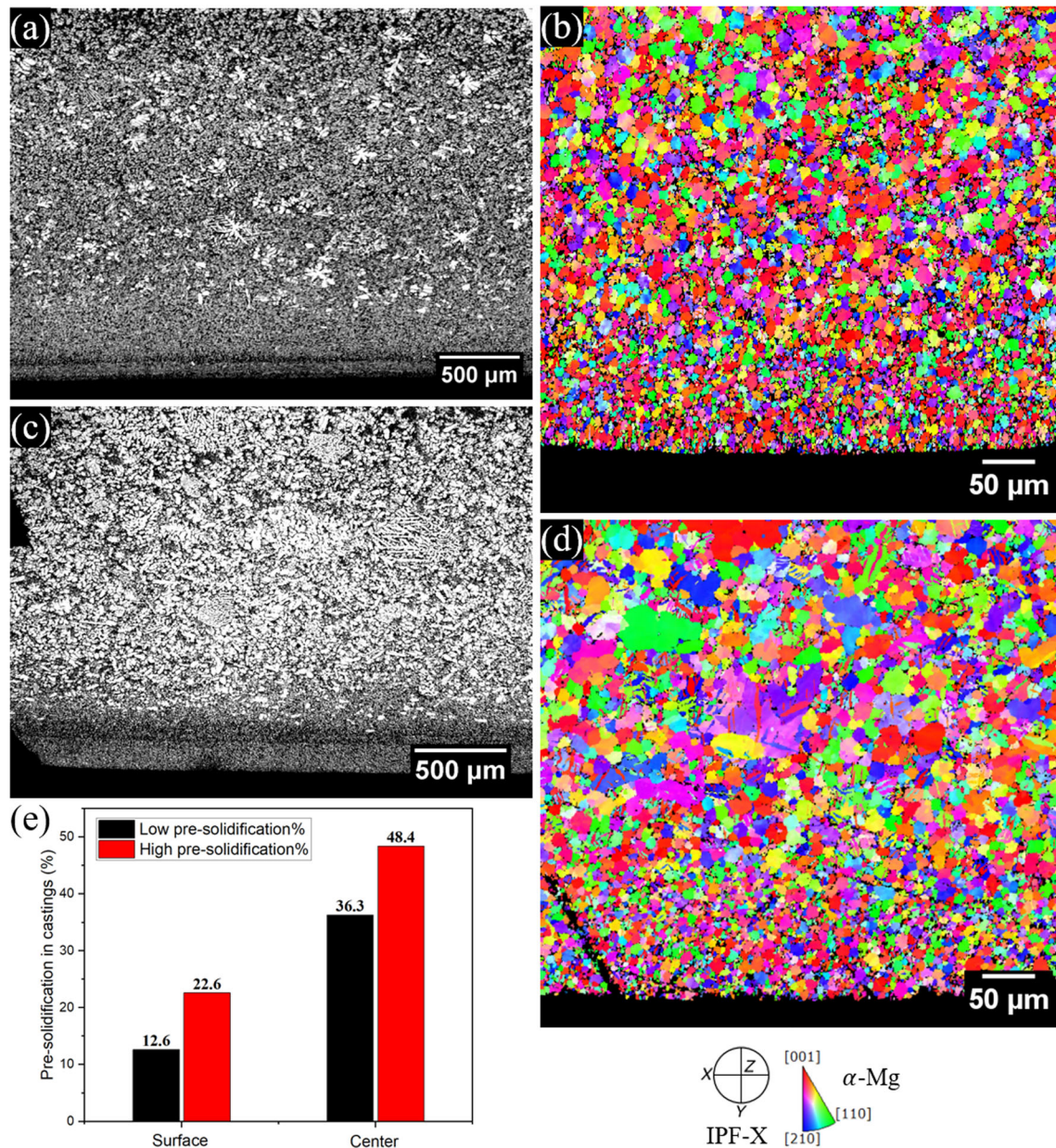|	Grain Size (min) (μm)	Grain Size (max) (μm)	Grain Size (Av.) (μm)	SDAS (Av.) (μm)
In-Cavity Grains	—	—	16.5 ± 1.0	3.6 ± 0.3
In Cold Flakes	67.5	284.6	174.1 ± 13.5	7.9 ± 0.5
Fragmented ESCs	33.6	285.5	131.1 ± 23.9	18.3 ± 0.9
Entrapped ESCs	223.5	554.6	353.8 ± 71.9	18.0 ± 3.5
In Segregation Pockets	—	—	46.2 ± 2.5	3.6 ± 0.4

Fig. 4—(*a*) through (*d*) Comparison of externally solidified crystals (ESCs) in the near-surface region from bars A and bars B. (a) and (b) a low pre-solidification content sample (bar B). (c) and (d) a high pre-solidification content sample (bar A).(*e*) Area pct of pre-solidified material (ESCs and cold flakes) at the surface and centre for high and low pre-solidification content samples.

zone, the liquid drawn-in behind moving cold flakes is rich in Al, La and Ce solute, resulting in positive macrosegregation.

To further interpret the different regions of α-Mg microstructure induced by shot sleeve pre-solidification, the dendrite arm spacing *vs* grain size is plotted for multiple α-Mg grains from each feature in Figure 7(a), producing an equiaxed grain morphology map.[53,54] Micrographs of the range of α-Mg grain morphologies are shown in Figure 7(c), where the in-cavity solidified grains span the globular-rosette-dendrite morphology transition. To quantify this transition, the surface factor, *Z*, defined in Eq. [1] was used.[55–57]

$$Z = \frac{c^2}{4\pi A} \qquad [1]$$

Where *c* is the perimeter of the grain and A is the area of the grain, both measured on 2D sections with ImageJ software. With this shape factor, a spherical grain has *Z* = 1 and *Z* increases with increasing local curvature and branching. From optical micrographs such as those in Figure 7(c), the measured surface factor, *Z*, is plotted against the ratio of the grain size/dendrite arm spacing (DAS) in Figure 7(b).
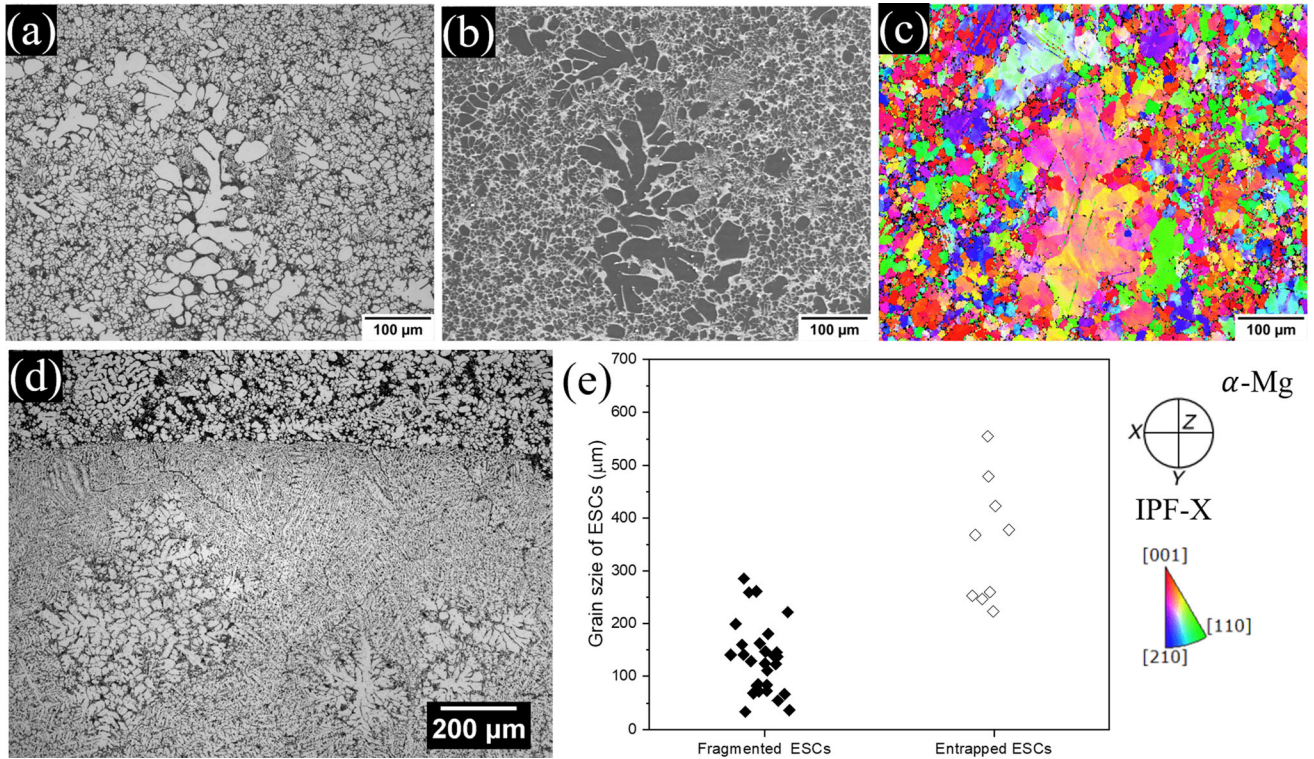
Fig. 5—Effects of cold flakes on externally solidified crystals (ESCs). (*a*) through (*c*) OM, SEM and EBSD (IPF-X map) of a typical fragmented ESC surrounded by in-cavity solidified grains. (*d*) An example of ESCs entrapped in a cold flake. (*e*) Summary of grain size of fragmented ESCs and entrapped ESCs.
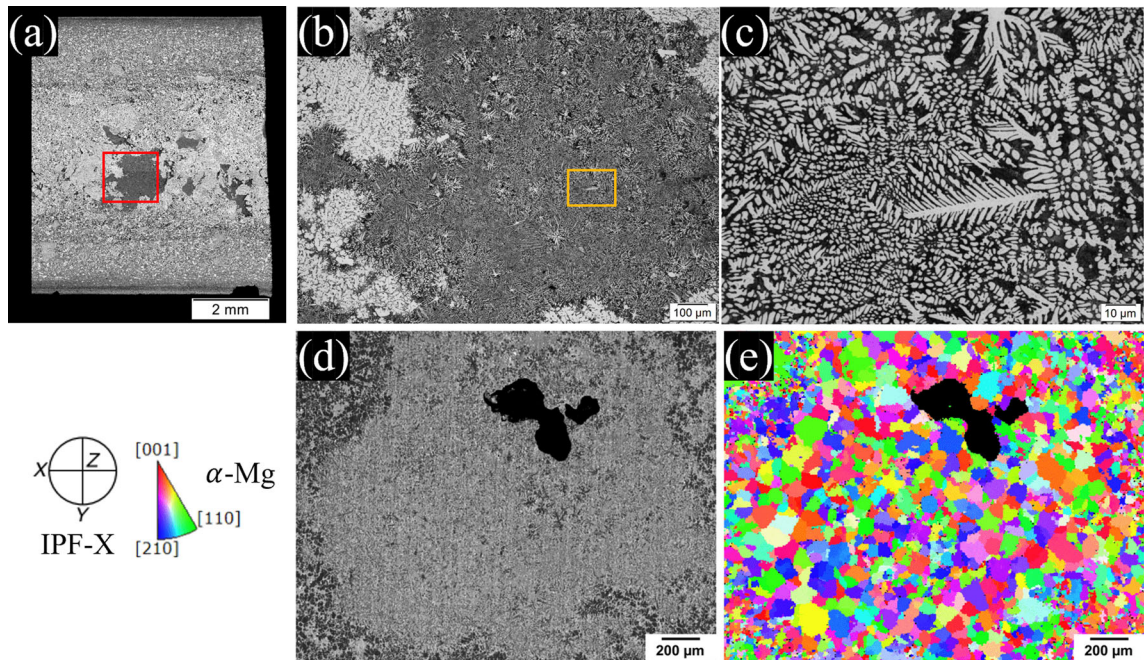

Fig. 6—Microstructure within segregation pockets. (*a*) through (*c*) OM images of one positive segregation pocket at various magnifications. (*d*) and (*e*) SEM image and EBSD map of the α-Mg grain structure in a segregation pocket containing a large pore (black).

Using the definition that globular grains have no branches, rosette grains have only primary arms, and dendritic grains have secondary arms, it was found that the Z factor of globular grains is between 1.0 and 2.0, the Z factor of rosette grains varies between 2.1 and 5.3 depending on the shape and length of the primary dendrite arms, and most equiaxed dendritic grains have larger Z factor because secondary dendrite arms
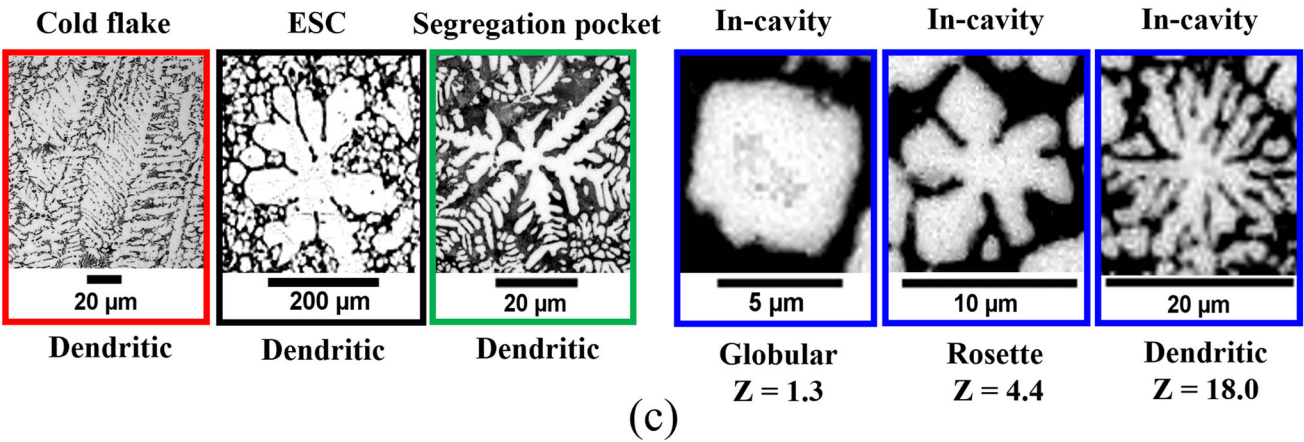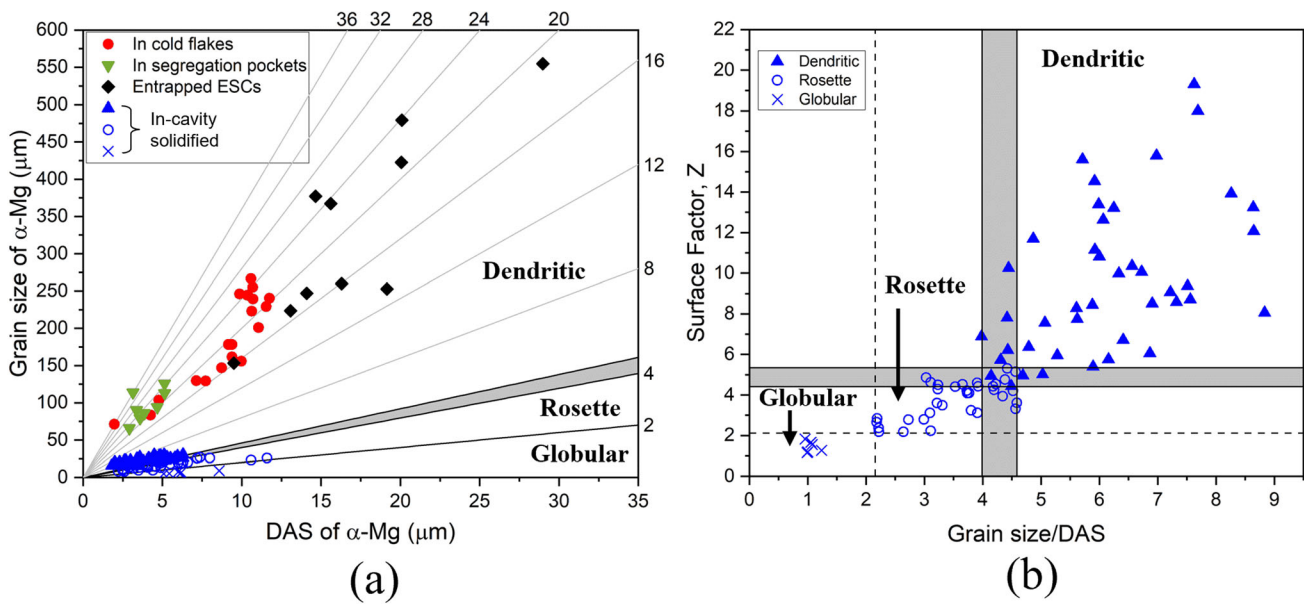
Fig. 7—Variations in α-Mg grain morphology. (*a*) Equiaxed grain morphology map (grain size *vs* dendrite arm spacing, DAS) for different microstructural features. (*b*) Z shape factor of α-Mg *vs* the grain size/DAS ratio of in-cavity solidified grains showing the globular-rosette-dendritic morphology transition. The grey area in (a) and (b) is a transition region where rosette and dendritic morphologies co-exist. (*c*) Example micrographs from the range of α-Mg grain morphologies.

significantly increase the perimeter for a given grain area. Moreover, an overlapping range was found among the rosette and dendritic grains when Z is between 4.4 and 5.3 and the grain size/DAS ratio is between 4.0 to 4.6, where some rosette and dendritic grains have similar Z value and ratio, as shaded in grey in Figure 7(b). Using these values for the grain size / DAS ratio, three different regions are divided in Figure 7(a) using a gradient of 4.0 to 4.6 for the rosette-to-dendritic transition, and a gradient of 2 for the globular-to-rosette transition. These gradient values are similar to those measured for grain morphologies in aluminium alloys in past work.[53] This indicating that the geometric ratios for grain morphology transitions are similar for hexagonal and cubic dendrites.

From the grain morphology map in Figure 7(a), we see the data fall into two groups. The first group includes ESCs and the grains in cold flakes and segregation pockets (black, red and green datapoints)

which are all dendritic and share a similar near-linear relationship between grain size and SDAS. Note that, on average, the ratio of the grain size to SDAS (indicated with gradient lines) increases as the grain size decreases, *i.e.* in the first group, the smaller grains generally have more intricately branched dendrites. These results are similar to a study by Easton *et al.*[53] on the effects of cooling rate in aluminium alloys where, for a given composition, increasing the cooling rate decreased the grain size and increased the ratio of grain size to SDAS. Thus, the results in the grain morphology map in Figure 7(a) can be interpreted qualitatively in terms of changes in the local cooling rate:

The entrapped ESCs nucleated and grew in the bulk liquid within the shot sleeve at relatively low cooling rate. The cold flakes solidified on the cold shot sleeve wall where the cooling rate was higher. Segregation pockets solidified in the main die cavity near to the injected cold flakes where the cooling rate was even

higher than in the shot sleeve but have a distinctly different morphology to the main in-cavity solidified grains as discussed in the next paragraph. In Figure 7(a), we also see overlap between some of the black, red and green datapoints. For the grains within cold flakes, it was shown in Figure 3 that the grain size and SDAS depend on cooling rate variations due to how far a grain solidified from the shot sleeve wall. More generally, the overlapping datapoints are due to the complex heat flow conditions in HPDC that change with both position and time.[58–60] Note in Figure 7(a) that the only ESCs plotted are entrapped ESCs because they remain as whole dendrites during die filling. If other ESCs were plotted, they would have a similar SDAS but span a wide range of grain size due to fragmentation during die filling (see Figure 5(e)).

The second group in the grain morphology map in Figure 7(a) are the blue datapoints that include all the in-cavity solidified grains except those in cold-flake-induced segregation pockets. This group spans the globular-rosette-dendritic transition and is markedly different to the first group in that the blue in-cavity solidified grains formed at the highest cooling rate and yet had the smallest ratio of grain size to DAS. The difference can be understood from the cooling and flow conditions experienced when liquid enters the thin die cavity at high velocity. The early stages of solidification of these grains involves both fast cooling (initially with heat transfer coefficient on the order 10^4 Wm^{-2} K^{-1}[58,61] and cooling rate >1000 K s^{-1}[62]) and strong forced convection (due to highly turbulent flow during die filling[59]). This combination gives a high number density of growing grains from nucleation events and fragmentation[63] that can be sufficiently high that solute fields overlap before growth becomes dendritic and results in both a very fine cast grain size and morphologies that can be nondendritic.[64,65] This results in the distinctly different location on the morphology map of most in-cavity solidified grains compared with grains that began their solidification in the shot sleeve. The exception are the grains in segregation pockets that solidified in the main die cavity but have a morphology in the first group that includes ESCs and the grains in cold flakes. This can be understood from the different time when segregation pockets start solidifying: *i.e.* the liquid in segregation pockets was drawn-in after the main in-cavity solidified grains had started solidifying and when heat transfer was slower.

B. *The Role of Pre-solidification on* $Al_{11}RE_3$ *Phase*

The morphology and volume fraction of $Al_{11}RE_3$ in the α-Mg + $Al_{11}RE_3$ eutectic was also influenced by pre-solidification in the shot sleeve. Figures 8(a) and (d) shows the reconstructed 3D morphology and a deep-etched image of $Al_{11}RE_3$ in a typical in-cavity solidified region. The $Al_{11}RE_3$ has a fine interconnected structure with a mostly fibrous eutectic morphology with smaller regions of lamellar morphology. This is the typical morphology of $Al_{11}RE_3$ in HPDC AE44 reported in the References 10, 31, 66, 67, and 68.
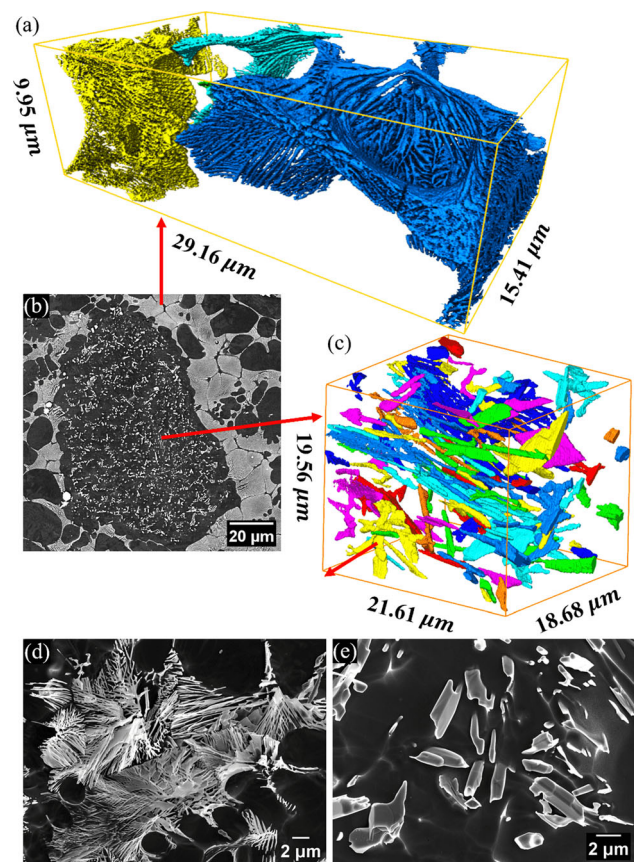

Fig. 8—(a) 3D eutectic $Al_{11}RE_3$ skeleton in the low pre-solidificaion pct in-cavity region. (b) BSD image contained a cold flake surrounding by in-cavity grains. (c) 3D morphology of eutectic $Al_{11}RE_3$ in cold flakes. (d) Deep-etched image in the low pre-solidificaion pct in-cavity region. (e) Deep-etched image in cold flakes.

Figures 8(c) and (e) overviews the typical features of $Al_{11}RE_3$ within cold flakes as a reconstructed 3D morphology and an SEM image after deep-etching. Compared with in-cavity solidified regions, these $Al_{11}RE_3$ within cold flakes are coarser and have a non-continuous morphology. The $Al_{11}RE_3$ in Figures 8(c) and (e) is similar to the $Al_{11}RE_3$ reported for gravity cast AE44 by Le *et al.*,[9] consistent with shot sleeve solidification conditions being similar to gravity casting.

The $Al_{11}RE_3$ in positive segregation pockets had another distinct morphology that is overviewed in Figures 9(a) through (d). From the reconstructed 3D morphology, it can be seen that $Al_{11}RE_3$ is relatively coarse and thick and has a semi-continuous morphology. This intermediate morphology between the main in-cavity solidified $Al_{11}RE_3$ and the cold-flake $Al_{11}RE_3$ is consistent with the segregation pockets solidifying at a cooling rate intermediate between these two regions as implied by Figure 7(a). Positive segregation pockets also often contained large hollow rods of $Al_{11}RE_3$, as shown in Figures 9(b) and (c), that resemble the morphology of $Al_{11}RE_3$ when it is a primary solidification phase in high RE pct Al–RE alloys.[69–71]

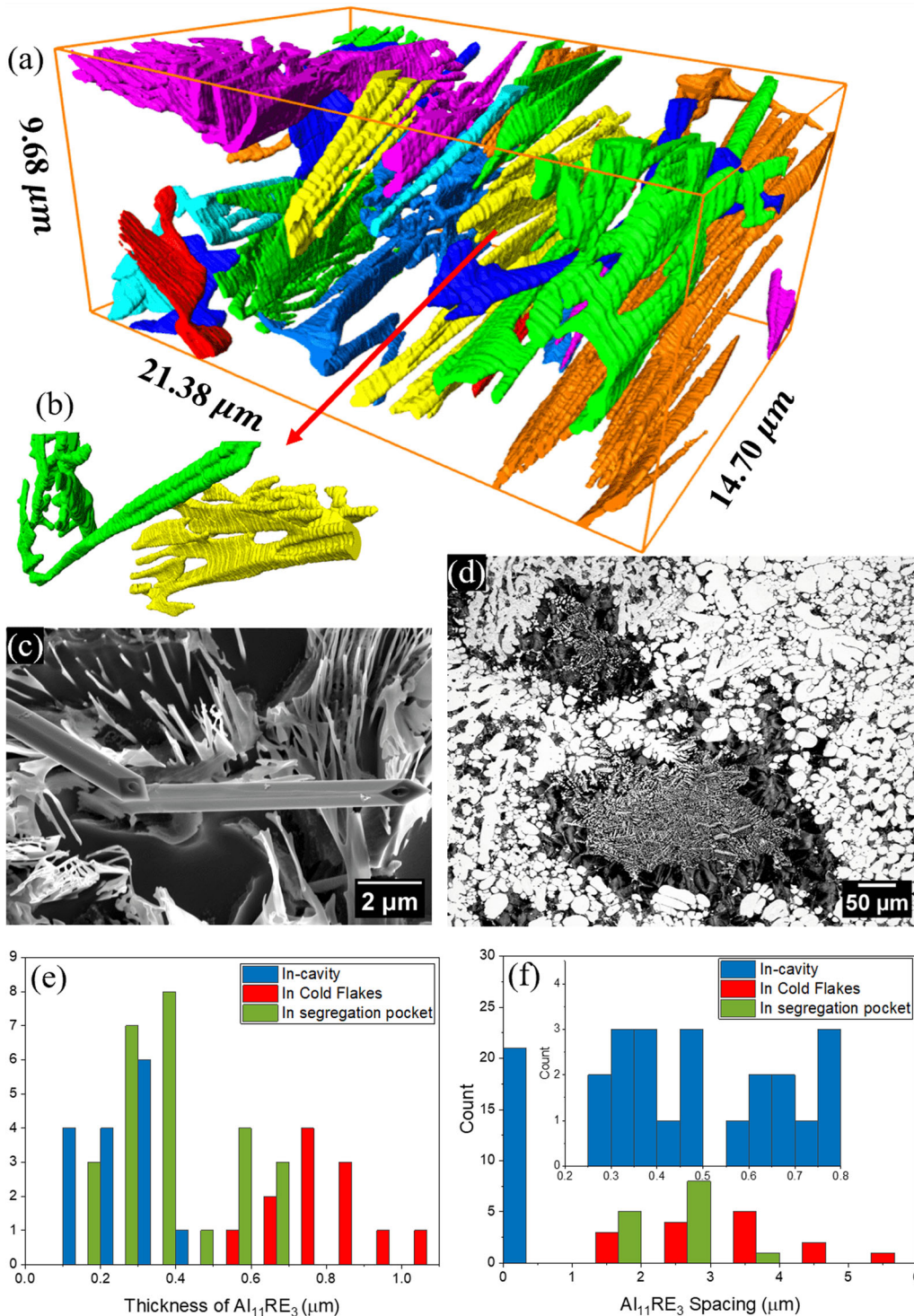Fig. 9—(a) 3D morphology of eutectic $Al_{11}RE_3$ in the segregation pocket. (b) a selected rod-like α-$Al_{11}RE_3$. (c) Deep-etched SEI image of straw-like $Al_{11}RE_3$. (d) OM image of segregation pocket at low magnification. (e) Thickness of $Al_{11}RE_3$ in different features. (f) $Al_{11}RE_3$ spacing in different features.

To quantify the $Al_{11}RE_3$ in the different regions, Figures 9(e) and (f) are hisotgrams plotting the distribution of eutectic $Al_{11}RE_3$ thickness and spacing in each feature and Table III summarizes the mean ± standard deviation values. The $Al_{11}RE_3$ has nano-scale thickness and spacing in the low pre-solidification

regions. The $Al_{11}RE_3$ in the cold flakes is three times thicker, and the spacing is six times wider than that in the low pre-solidification content regions. The $Al_{11}RE_3$ in the segregation pockets has a length scale intermediate between the cold flakes and the in-cavity solidified regions.

Table III. Thickness Spacing, and Volume Fraction of $Al_{11}RE_3$ in each Features

	$Al_{11}RE_3$ Thickness (μm)	$Al_{11}RE_3$ Spacing (μm)	Volume Fraction (pct)
In-Cavity Solidified	0.26 ± 0.05	0.51 ± 0.08	5.03
In Cold Flakes	0.78 ± 0.08	3.04 ± 0.55	3.94
In Segregation Pockets	0.36 ± 0.09	2.10 ± 0.34	7.37

'±' calculated by the standard deviation

Table III also shows significant changes in the volume fraction of $Al_{11}RE_3$ in the different regions. This is a consequence of macrosegregation causing a different average composition in the different regions. Specifically, cold flakes solidified from liquid of composition of the whole alloy (Table I). In-cavity solidified regions solidified from liquid that was richer in Al, La and Ce solute because shot sleeve pre-solidification increased the composition of the remaining liquid prior to injection. Segregation pockets solidified from even more solute-rich liquid because liquid was drawn-in to these pockets later during the solidification process. Thus, we would expect the volume fraction of $Al_{11}RE_3$ to vary according to cold flakes < standard in-cavity solidified regions < in segregation pockets, as measured in Table III.

C. Tensile Properties

Figure 10(a) plots the true stress-strain curves of 20 as-cast and 20 T5 (250 °C for 4 hours) heat-treated samples and the tensile properties are summarized in Table IV. From Figures 10(b) and (c) and Table IV, we see that samples with high pre-solidification content had slightly lower 0.2 pct yield stress and significantly reduced fracture strain and UTS, by 37 and 12 pct respectively, compared with low pre-solidification content samples. These findings on magnesium alloy AE44 are similar to previous work on Al–Si alloys.[20–22] Moreover, the 0.2 pct yield stress of AE44-2 was improved with the T5 heat treatment by about 11 pct. Recent research has shown this is due to the precipitation of Mn-bearing intermetallics in the α-Mg matrix during the heat treatment,[36,72,73] which were identified as $Al_{10}Mn_7RE_2$ nano-scale particles on Ce-rich clusters in Reference 42

The slight reduction in 0.2 pct yield stress in samples with a high pre-solidification content *vs* those with a low pre-solidification content is likely due to the larger microstructural length scale in samples with high pre-solidification content (Figure 7(a), Tables II and 3) and due to the presence of a non-bonded interface between cold flakes and the in-cavity solidified material. Examining Figure 10(a), we see that the apparent Young's modulus (the initial slope) is negligibly changed by pre-solidification. This indicates that the load bearing area is not significantly reduced by the presence of cold flakes, so it is likely that the fraction of non-bonded interface is much smaller than the fraction of cold flakes. A small fraction of pre-existing cracks associated with a non-bonded interface does not strongly affect the 0.2 pct yield stress which is determined by the microstructure-dependent critical resolved shear stress (CRSS) for dislocation slip.

Figures 11(a) and (c) are OM and SEM images of the fracture surface of one high pre-solidification content

sample and Figures 11(b) and (d) are an OM image and an EBSD α-Mg orientation map of the etched longitudinal section of the same sample. Fracture has occurred at the boundary between a cold flake and the in-cavity solidified microstructure, and the non-bonded interface is labelled with yellow arrows. A clear crack propagation at the non-bonded interface is shown in a tensile tested sample, in Figures 11(e) and (f). It can be seen that the non-bonded interface in cold flakes acts as a pre-existing crack. During tensile testing, strain would accumulate at these pre-existing cracks, and lead to the earlier tensile failure.

In castings and other solidification processing routes, the variability in tensile ductility is usually quantitatively correlated to the area fraction of defect at the fracture surface.[74–79] Lee *et al.*[76] have demonstrated this relationship for HPDC AE44 containing different levels of porosity. To explore the role of cold flakes on tensile properties of AE44, we measured the area fraction of defect (cold flakes and pores) at the fracture surface in both stereo-OM and SEI, as shown in Figures 12(a) and (b). The data are plotted in Figure 12(c) where samples with discernable porosity on the fracture surface are plotted as open symbols and samples with only cold flakes (no discernable porosity) are plotted as filled symbols. Figure 12(c) shows the negative correlation between the area fraction of cold flakes at the fracture surface and the ductility. This is partly because the larger the cold flake, the larger the non-bonded interface, and a larger pre-existing crack leads to an earlier tensile failure. For samples with defect area less than 2 pct, the data fall close to the relationship between porosity and ductility measured by Lee *et al.*,[76] which is plotted as a dotted line in Figure 12(c). For samples with defect area more than 2 pct, the data follow a more shallow curve. These results indicate that cold flakes are less deleterious than porosity for a given area fraction of defect which is reasonable since not all of a cold flake is a non-bonded interface. However, cold flakes can occupy a large area fraction (up to 31 pct in this work) and, therefore, can strongly degrade the tensile ductility.

Excessive pre-solidification and cold flakes should be prevented by maintaining a sufficiently high metal temperature in the shot sleeve and minimising the amount of pre-solidification that enters the die through die design and process optimisation.
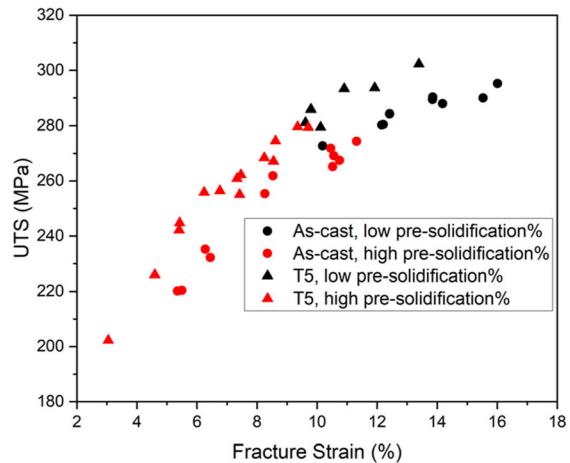
IV. CONCLUSION

EBSD, FIB-tomography and selective etching techniques have been used to gain new insights into the effects of shot sleeve pre-solidification on the microstructure and tensile properties of HPDC AE44-2. The following conclusions can be drawn:
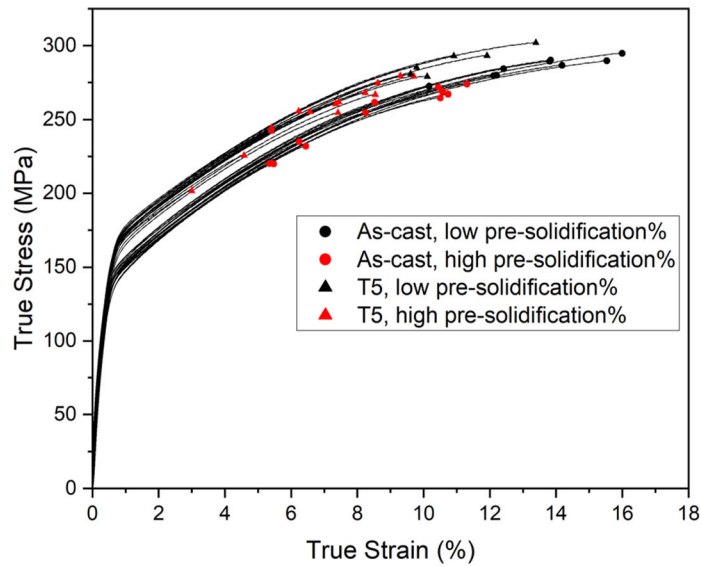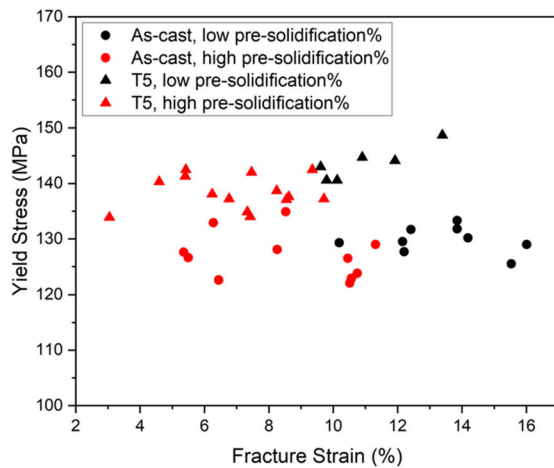
Fig. 10—Tensile behaviour of the HPDC AE44. (*a*) True stress-strain curves from 20 as-cast and 20 T5 samples. (*b*) 0.2 pct yield stress *vs* fracture strain data. (*c*) UTS *vs* fracture strain data. Red datapoints are from high pre-solidification content bars (bar A) (Color figure online).

A high pre-solidification content induces a range of microstructural features in addition to externally solidified crystals (ESCs) and cold flakes, including ESCs entrapped in cold flakes, large positive segregation pockets, porosity and a highly heterogeneous α-Mg microstructure. These features also contained coarse eutectic $Al_{11}RE_3$ intermetallic phase instead of the fine fibrous α-Mg + $Al_{11}RE_3$ eutectic in samples with low pre-solidification content. The part of cold flakes that was initially in contact with the lubricated shot sleeve wall usually had a non-bonded interface with the surrounding material in the final casting.

The size and morphology of α-Mg grains in the different features has been rationalised using an equiaxed grain morphology map (a plot of grain size *vs* dendrite arm spacing). Entrapped ESCs and α-Mg grains in cold flakes and segregation pockets followed a similar grain size *vs* dendrite arm spacing relationship that is consistent with the cooling rate being lowest for ESCs and highest for segregation pockets. The remaining α-Mg that solidified in the die cavity followed a different grain size *vs* dendrite arm spacing relationship and spanned the globular-rosette-dendritic transition due to the high number density of nucleation and fragmentation events during die filling.

A high fraction of shot sleeve pre-solidification was detrimental to tensile properties. The yield stress was slightly reduced due to the increased microstructural length scale. The ductility and UTS was more substantially reduced by 37 and 12 pct, respectively. Cold flakes were usually found at the fracture surface where a non-bonded interface acted as a pre-existing crack, which leads to the earlier tensile failure.

Table IV. Summary of Tensile Properties of AE44-2

		0.2 pct Yield Stress (MPa)	Fracture Strain (Pct)	UTS (MPa)	No. of Test
As Cast	low p.s.	129.8 ± 1.7	13.4 ± 1.3	285.6 ± 5.0	9
	high p.s.	127.0 ± 2.7	8.5 ± 1.5	252.1 ± 13.4	11
T5 (250 °C for 4 h)	Low p.s.	143.6 ± 2.9	11.0 ± 1.4	289.3 ± 8.3	6
	high p.s.	138.4 ± 1.7	7.0 ± 1.1	255.3 ± 11.8	14

'p.s.' = pre-solidification.
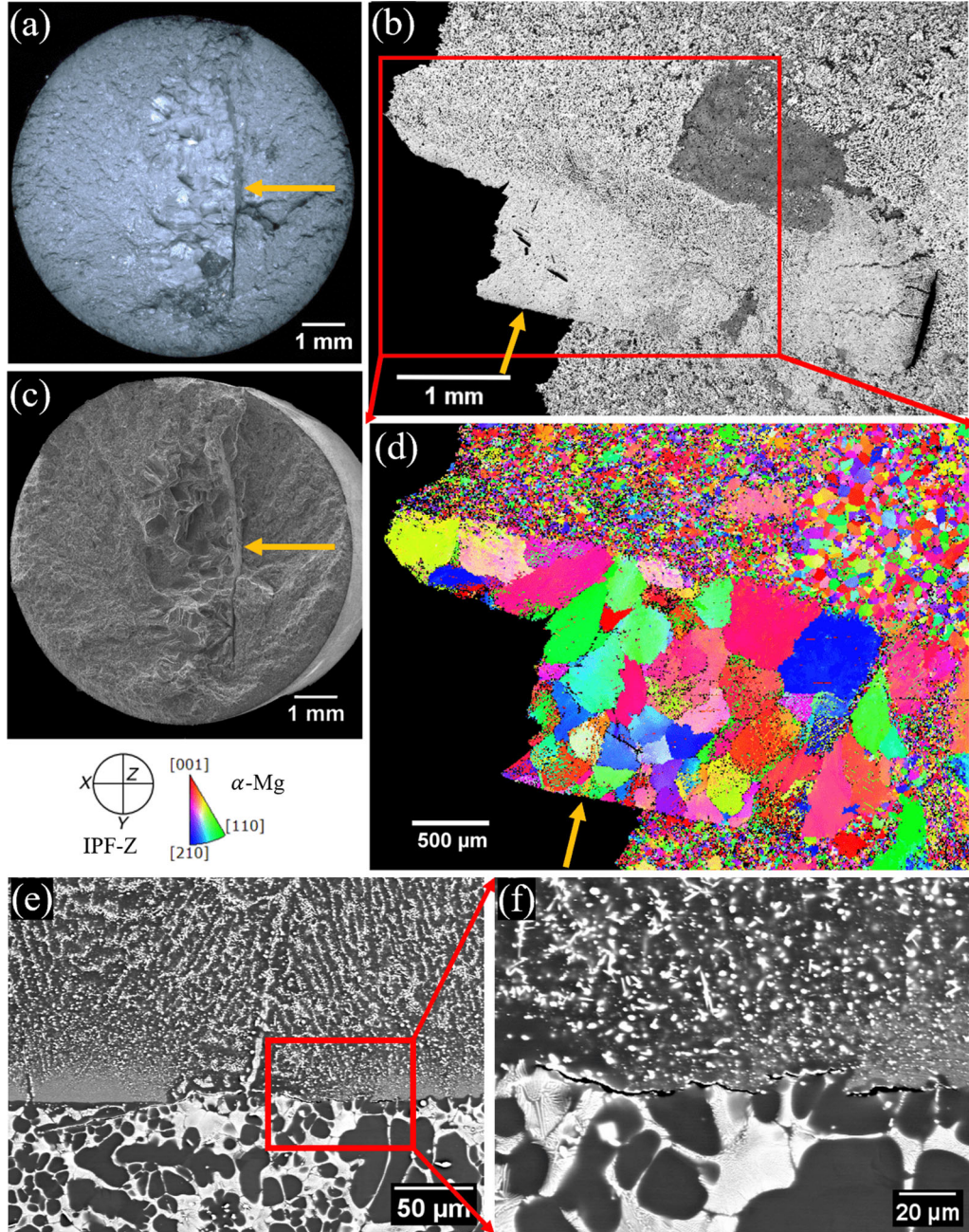
Fig. 11—Microstructure near the fracture surface of a sample with a high pre-solidification content (bar A). (*a*) Stereograph of the fracture surface. (*b*) OM image of a longitudinal section through fracture surface. (*c*) SE image of the fracture surface. (*d*) IPF-Z EBSD orientation map of a region in (b) containing a cold flake, segregation pocket and in-cavity solidified grains. (*e*) OM image of a cold flake and surrounding material. (*f*) higher magnification image of a region in (e) showing cracks at the non-bonded interface.
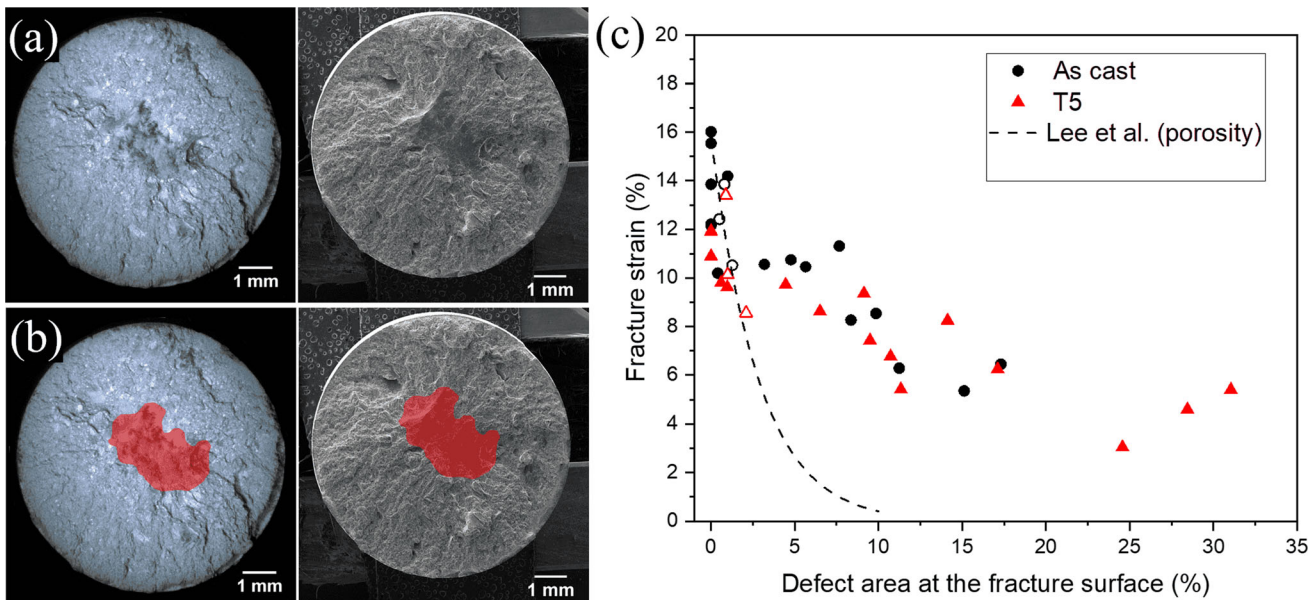
Fig. 12—Relationship between cold flakes and tensile ductility. (*a*) and (*b*) Typical fracture surface in a high pre-solidification pct sample (bar A). (a) contains both a stereograph and an SEM image. (b) highlights the defect area in red. (*c*) Fracture strain *vs* the defect area fraction at the fracture surface. Open symbols indicate samples where significant porosity was observed on the fracture surface. Filled symbols are samples with only cold flakes. The expression of Lee *et al.*[76] for fracture strain *vs* porosity in HPDC AE44 is plotted as a dashed line: $e = 15.8(1 - f)^{34.7}$.

Quantification of defects on fracture surfaces showed that the ductility of AE44-2 was negatively correlated to the area fraction of defect at the fracture surface. For a given area fraction of defect, cold flakes were less deleterious to tensile ductility than porosity. However, cold flakes can be much larger than pores and, thus, can severely degrade tensile properties.

CONFLICT OF INTEREST

On behalf of all authors, the corresponding author states that there is no conflict of interest.

OPEN ACCESS

REFERENCES

1. M.K. Kulekci: *Int. J. Adv. Manuf. Technol.*, 2008, vol. 39, pp. 851–65.
2. A.A. Luo: *J. Mag. Alloys*, 2013, vol. 1(1), pp. 2–22.
3. W.P. Sequeira, G. L. Dunlop, and M.T. Murray: *Proceedings of the Third International Magnesium Conference*, 1996, pp. 63–73.
4. A.L. Bowles, J.R. Griffiths, and C.J. Davidson: *Mag. Technol.*, 2001, vol. 2001, pp. 161–68.
5. T. Liang, C.E. Mobley, and N. Tsumagari: *Die Casting Congress & Exposition*, 2002.
6. H.I. Laukli, O. Lohne, S. Sannes, H. Gjestland, and L. Arnberg: *Int. J. Cast Met. Res.*, 2003, vol. 16(6), pp. 515–21.
7. C.M. Gourlay, H.I. Laukli, and A.K. Dahle: *Metall. Mater. Trans. A*, 2007, vol. 38A, pp. 1833–44.
8. W. Sun, X. Shi, E. Cinkilic, and A.A. Luo: *J. Mater. Sci.*, 2016, vol. 51, pp. 6287–94.
9. T. Le, Q. Wei, J. Wang, P. Jin, M. Chen, and J. Ma: *Mater. Res. Express*, 2020, vol. 7(11), p. 116513.
10. Y. Xia, J. Zheng, J. Chen, Y. Zhang, R. Shi, H. Zhou, et al.: *Metall. Mater. Trans. A*, 2021, vol. 52A, pp. 2274–86.
11. T.T. Zhang, W.B. Yu, C.S. Ma, W.T. Chen, L. Zhang, and S.M. Xiong: *J. Mag. Alloys*, 2023, vol. 11(9), pp. 3141–50.
12. W.G. Walkington and D.M. Murray: *Die Casting Defects: Causes and Solutions*, 2015, pp. 147–50.
13. L. Wang, T. Nguyen, G. Savage, and C. Davidson: *Int. J. Cast Met. Res.*, 2003, vol. 16(4), pp. 409–17.
14. A. Bowles, K. Nogita, M. Dargusch, C. Davidson, and J. Griffiths: *Mater. Trans.*, 2004, vol. 45(11), pp. 3114–19.

15. X.B. Li, S.M. Xiong, and Z.P. Guo: *Mater. Sci. Eng. A*, 2015, vol. 633, pp. 35–41.
16. K. Dou, Y. Zhang, E. Lordan, A. Jacot, and Z. Fan: *Metall. Mater. Trans. A*, 2022, vol. 53A(8), pp. 3110–24.
17. H. Cao and M. Wessén: *Int. J. Cast Met. Res.*, 2005, vol. 18(6), pp. 377–84.
18. B.S. Wang and S.M. Xiong: *Trans. Non-ferrous Met. Soc. China*, 2011, vol. 21(4), pp. 767–72.
19. M.W. Wu, X.B. Li, Z.P. Guo, and S.M. Xiong: *China Foundry*, 2018, vol. 15(2), pp. 139–45.
20. A.K.M. Ahamed, H. Kato, K. Kageyama, and T. Komazaki: *Mater. Sci. Eng. A*, 2006, vol. 423(1–2), pp. 313–23.
21. C. Mobley, Y. Sahai, J. Brevick: The Ohio State University (US), unpublished research, 2003.
22. T. Komazaki, Y. Maruyama, and N. Nishi: *Imono*, 1995, vol. 67(4), pp. 258–64.
23. A.K.M. Ahamed and H. Kato: *Int. J. Cast Met. Res.*, 2008, vol. 21(1–4), pp. 162–67.
24. A. Kopper, A.K. Monroe: 2015 Die Casting Congress & Exposition, NADCA Transactions, 2015.
25. P. Paliani, L. Zalewski, J. Barreto, N. Tsumagari, J. Brevick, C. Mobley: NADCA Proceedings, 1995, pp. 149–55.
26. M. Gershenzon, P. Rohan, M. T. Murray: NADCA Transactions, 1999.
27. M. Okayasu, S. Wu, T. Hirayama, and Y.S. Lee: *Int. J. Cast Met. Res.*, 2018, vol. 31(5), pp. 308–16.
28. N. Tsumagari, T. Liang, J. Brevick, C.E. Mobley: Die Casting Congress & Exposition, NADCA Transactions, 2001, pp. 251–56.
29. D. R. Gunasegaram, M. Givord, R. O'Donnell, B. Finnin: NADCA Transactions, 2008.
30. P. Bakke, K. Pettersen, and H. Westengen: *Mag. Technol.*, 2003, vol. 2003, pp. 171–76.
31. P. Bakke, H. Westengen: *Magnesium Technology*, 2005, pp. 313–18.
32. B.R. Powell, V. Rezhets, M.P. Balogh, and R.A. Waldo: *Jom*, 2002, vol. 54, pp. 34–38.
33. P. Bakke, H. Westengen, S. Sannes, D. Albright: SAE Technical Paper Series, 2004, 01(0655).
34. M. Pekguleryuz and M. Celikin: *Int. Mater. Rev.*, 2010, vol. 55(4), pp. 197–217.
35. A.A. Luo: *Magnesium Technology*, 2000, vol. 2000, pp. 89–98.
36. S. Zhu, T.B. Abbott, J.F. Nie, H.Q. Ang, D. Qiu, K. Nogita, and M.A. Easton: *J. Mag. Alloys*, 2021, vol. 9(5), pp. 1537–45.
37. M.A. Easton, S. Zhu, T.B. Abbott, M. Dargusch, M. Murray, G. Savage, et al.: *Adv. Eng. Mater.*, 2016, vol. 18(6), pp. 953–62.
38. S. Zhu, M.A. Easton, T.B. Abbott, J.F. Nie, M.S. Dargusch, N. Hort, and M.A. Gibson: *Metall. Mater. Trans. A*, 2015, vol. 46A, pp. 3543–54.
39. Y. Jiao, J. Zhang, L. He, M. Zhang, F. Jiang, W. Wang, et al.: *Adv. Eng. Mater.*, 2016, vol. 18(1), pp. 148–55.
40. S. Fan, X. Wang, G.G. Wang, J.P. Weiler: IntechOpen, 2023.
41. Y. Li, J. Wang, H. Ma, Z. Zhen, Y. Liu, H. Zhang, and P. Jin: *Mater. Res. Express*, 2022, vol. 9(2), p. 020005.
42. T.M. Schwarz, W. Yu, H. Zhan, B. Gault, C.M. Gourlay, and I. McCarroll: *Scripta Mater.*, 2023, vol. 232, p. 115498.
43. J. Schindelin, I. Arganda-Carreras, E. Frise, V. Kaynig, M. Longair, T. Pietzsch, and A. Cardona: *Nat. Methods*, 2012, vol. 9(7), pp. 676–82.
44. C.H. Cáceres, J.R. Griffiths, A.R. Pakdel, and C.J. Davidson: *Mater. Sci. Eng. A*, 2005, vol. 402(1–2), pp. 258–68.
45. X. Li, S.M. Xiong, and Z. Guo: *Mater. Sci. Eng. A*, 2016, vol. 500, pp. 216–25.
46. A.K. Dahle, Y.C. Lee, M.D. Nave, P.L. Schaffer, and D.H. StJohn: *J. Light. Met.*, 2001, vol. 1(1), pp. 61–72.
47. H.I. Laukli, C.M. Gourlay, A.K. Dahle, and O. Lohne: *Mater. Sci. Eng. A*, 2005, vol. 413, pp. 92–97.
48. T.Z. Kattamis: *Trans. Metall. Soc. AIME*, 1967, vol. 239, pp. 1504–11.
49. M.C. Flemings: *Metall. Mater. Trans. B*, 1974, pp 246–48.
50. K. Pettersen, O. Lohne, and N. Ryum: *Metall. Trans. A*, 1990, vol. 21, pp. 221–30.
51. D. Dubé, A. Couture, Y. Carbonneau, M. Fiset, R. Angers, and R. Tremblay: *Int. J. Cast Met. Res.*, 1998, vol. 11(3), pp. 139–44.
52. S.J. Norris, I.M. Brooks, G. De Leeuw, A. Sirevaag, C. Leck, B.J. Brooks, et al.: *Ocean Sci.*, 2011, vol. 7(1), pp. 129–39.
53. M. Easton, C. Davidson, and D. StJohn: *Mater. Trans.*, 2011, vol. 52(5), pp. 842–47.
54. C.J. Lin, L. Peng, J.W. Xian, Q. Li, and C.M. Gourlay: *J. Alloys Compd.*, 2023, vol. 938, p. 168571.
55. E. Tzimas and A. Zavaliangos: *Mater. Sci. Eng. A*, 2000, vol. 289(1–2), pp. 217–27.
56. H. Ishida, Y. Natsume, and K. Ohsasa: *ISIJ Int.*, 2009, vol. 49(1), pp. 37–43.
57. K. Ohsasa, Y. Natsume, T. Sekiya, and T. Hatayama: *IOP Conf. Ser.*, 2015, vol. 84(1), p. 012033.
58. Z.P. Guo, S.M. Xiong, B.C. Liu, M. Li, and J. Allison: *Metall. Mater. Trans. A*, 2008, vol. 39A, pp. 2896–2905.
59. K. Dou, E. Lordan, Y.J. Zhang, A. Jacot, and Z.Y. Fan: *J. Manuf. Process.*, 2020, vol. 60, pp. 435–46.
60. E. Lordan, Y. Zhang, K. Dou, A. Jacot, C. Tzileroglou, S. Wang, et al.: *Metals*, 2022, vol. 12(10), p. 1575.
61. W.B. Yu, S. Liang, Y.Y. Cao, X.B. Li, Z.P. Guo, and S.M. Xiong: *China Foundry*, 2017, vol. 14, pp. 258–64.
62. R. Helenius and O. Lohne: *Int. J. Metalcast.*, 2015, vol. 9, pp. 51–59.
63. M.C. Flemings: *Mater. Trans.*, 2005, vol. 46(5), pp. 895–900.
64. R.A. Martinez, A. Karma, and M.C. Flemings: *Metall. Mater. Trans. A*, 2006, vol. 37A, pp. 2807–15.
65. G.I. Eskin, D.G. Eskin: in *Proceedings of the 12th International Conference on Aluminium Alloys*, 2010, pp. 683–45.
66. G. Pettersen, H. Westengen, R. Høier, and O. Lohne: *Mater. Sci. Eng. A*, 1996, vol. 207(1), pp. 115–20.
67. T. Rzychoń, A. Kielbus, J. Cwajna, and J. Mizera: *Mater Charact*, 2009, vol. 60(10), pp. 1107–13.
68. S. Zhu, C. Wong, M.J. Styles, T.B. Abbott, J.F. Nie, and M.A. Easton: *Mater Charact*, 2019, vol. 156, p. 109839.
69. Z. Cao, G. Kong, C. Che, Y. Wang, and H. Peng: *J. Rare Earths*, 2017, vol. 35(10), pp. 1022–28.
70. Y. Guo, J. Hu, Q. Han, B. Sun, J. Wang, and C. Liu: *J. Alloys Compd.*, 2022, vol. 899, p. 162914.
71. Q. Wei, H. Wang, J. Li, X. Quan, W. Li, and B. Wang: *J. Alloys Compd.*, 2023, vol. 960, p. 170878.
72. S.M. Zhu, T.B. Abbott, M.A. Gibson, J.F. Nie, and M.A. Easton: *Mater. Sci. Eng. A*, 2016, vol. 656, pp. 34–38.
73. S.M. Zhu, T.B. Abbott, M.A. Gibson, J.F. Nie, and M.A. Easton: *Mater. Sci. Eng. A*, 2017, vol. 682, pp. 535–41.
74. C.H. Caceres and B.I. Selling: *Mater. Sci. Eng. A*, 1996, vol. 220(1–2), pp. 109–16.
75. A.M. Gokhale and G.R. Patel: *Mater Charact*, 2005, vol. 54(1), pp. 13–20.
76. S.G. Lee, G.R. Patel, A.M. Gokhale, A. Sreeranganathan, and M.F. Horstemeyer: *Mater. Sci. Eng. A*, 2006, vol. 427(1–2), pp. 255–62.
77. X. Teng, H. Mae, Y. Bai, and T. Wierzbicki: *Eng. Fract. Mech.*, 2009, vol. 76(8), pp. 983–96.
78. C.M. Laursen, S.A. DeJong, S.M. Dickens, A.N. Exil, D.F. Susan, and J.D. Carroll: *Mater. Sci. Eng. A*, 2020, vol. 795, p. 139922.
79. E. Lordan, J. Lazaro-Nebreda, Y. Zhang, K. Dou, P. Blake, and Z. Fan: *Mater. Sci. Eng. A*, 2020, vol. 778, p. 139107.

Publisher's Note Springer Nature remains neutral with regard to jurisdictional claims in published maps and institutional affiliations.